SCIENCE CHINA
Physics, Mechanics & Astronomy

• Article •
Special Topic: Fluid Mechanics

February 2013 Vol. 56 No. 2: 383–394
doi: 10.1007/s11433-012-4986-0

Numerical simulation of drop oscillation in AC electrowetting

LI XiaoLiang, HE GuoWei & ZHANG Xing*

The State Key Laboratory of Nonlinear Mechanics, Institute of Mechanics, Chinese Academy of Sciences, Beijing 100190, China

Received July 2, 2012; accepted October 25, 2012; published online January 21, 2013

In this paper, a "macroscopic-scale" numerical method for drop oscillation in AC electrowetting is presented. The method is based on a high-fidelity moving mesh interface tracking (MMIT) approach and a "microscopic model" for the moving contact line. The contact line model developed by Ren et al. [Phys Fluids, 2010, 22: 102103] is used in the simulation. To determine the slip length in this model, we propose a calibration procedure using the experimental data of drop spreading in DC electrowetting. In the simulation, the frequency of input AC voltage varies in a certain range while the root-mean-square value remains fixed. The numerical simulation is validated against the experiment and it shows that the predicted resonance frequencies for different oscillation modes agree reasonably well with the experiment. The origins of discrepancy between simulation and experiment are analyzed in the paper. Further investigation is also conducted by including the contact angle hysteresis into the contact line model to account for the "stick-slip" behavior. A noticeable improvement on the prediction of resonance frequencies is achieved by using the hysteresis model.

electrowetting, oscillation, contact line model, hysteresis, slip length

PACS number(s): 47.55.np, 47.55.dr, 47.11.Df

Citation: Li X L, He G W, Zhang X. Numerical simulation of drop oscillation in AC electrowetting. Sci China-Phys Mech Astron, 2013, 56: 383–394, doi: 10.1007/s11433-012-4986-0

Electrowetting (EW) is a phenomenon in which the wettability of a droplet on an insulator-coated electrode surface is modified by externally applying electrical voltages. This phenomenon originates from the electrostatic force, which is a direct consequence of the excess charge at the three-phase contact line [1]. A comprehensive review on EW, in both theory and experiment, was presented in the paper by Mugele and Baret [2]. EW can be used to manipulate small volume of liquid very fast and efficiently, with relatively low electrical potential and power consumption. Electrowetting on dielectric (EWOD) avoids the electrolysis of the aqueous solution in EW by coating the electrode surface with a thin dielectric layer. EWOD has been widely used in various applications, including microfluidics [3,4], liquid display [5,6], and microswitches [7,8].

Both DC and AC fields can be used in EW or EWOD. When a DC field is used, a new equilibrium state with a smaller contact angle will be reached after a spontaneous spreading process. If an AC field is used instead, more interesting and complex features are observed. At low-frequency AC excitation, the hydrodynamic response can follow the periodic change of the electric force at the contact line and the shape oscillation of droplet is observed. If the AC frequency exceeds a critical value for the hydrodynamic response, the droplet behaves just as if it is excited by a DC field. The final state of contact angle and shape depends only on the time-averaged value of the applied voltage. Recently, drop oscillation in AC EW at low frequencies (10–300 Hz) was studied by experiment and theory [9–11]. The experiments revealed that the drop oscillation became resonant at certain input AC frequencies and the pattern of shape oscillation was different at each resonance frequency. The theoretical models proposed in these works were able to predict some char-

*Corresponding author (email: zhangx@lnm.imech.ac.cn)

acteristics such as the resonance frequencies fairly well. The spreading of droplet in EW at a high AC frequency of 1 kHz was also studied [12]. It was found that the droplet behaved like being excited by a DC voltage. In another experiment, the oscillatory motion of droplet surface was observed up to about 8 kHz AC frequency [13]. They also showed a different flow pattern of EW in the high-frequency range of 35–256 kHz. Since this flow pattern was found to be very sensitive to the position of the needle (electrode) and the conductivity of the solution, it was believed to be a kind of electrohydrodynamic flow and was controlled by the electric-field distribution. More recent studies [14,15] suggested that this type of high-frequency flow originated mainly from the electrothermal effect. Several other groups also reported the existence of drop oscillations in AC EW [16–19]. As to the application side of drop oscillation, a significant enhancement of dye mixing was reported by Mugele et al. [20]. A thorough understanding of the nature of such oscillation (e.g., pattern of oscillation and resonance with respect to forcing frequency) can help optimize the mixing efficiency. Moreover, a fast and precise change in the shape of the meniscus is required in EW-based liquid lenses [21,22] and reflective displays [5].

In fact, drop oscillation is one fundamental problem in fluid mechanics and its study has a much longer history than that of EW. The first mathematical model for the oscillation of a free inviscid drop neglecting the external flow was proposed by Rayleigh [23]. This model was later extended by accounting for the external flow [24]. Efforts have also been made in the study of oscillation in partially constraint drops (such as sessile drops in contact with a solid substrate). An early theoretical study was motivated by the influence of liquid drop vibrations on crystal growth in microgravity [25]. The oscillation of gravity-flattened drops (puddles) on a vertically vibrated flat plate was studied by Noblin et al. [26]. They observed two different regimes of axisymmetric oscillations at different vibration amplitudes of the substrate: namely, type I with pinned contact line and type II with mobile contact line. The existence of non-axisymmetric (triplon) mode at high-amplitude excitations was also reported in another paper by Noblin et al. [27]. The resonant modes of an oscillating sessile drop on a substrate subjected to lateral vibration were studied by Dong et al. [28]. The stick-slip dynamics of an oscillated sessile drop subjected to vertical vibration were investigated recently by Fayzrakhmanova and Straube [29]. Their work focused on the contact angle hysteresis.

Some of the theoretical models have succeeded in predicting the drop spreading and oscillation in EW [8–10]. Usually in these models, the linearized flow field is analyzed instead of solving the full Navier-Stokes equations for the fluid. The simplifications made in the theoretical analysis, such as the drop of inertial term and small-parameter perturbation, will limit the range of validity. Compared to the theoretical models, significantly fewer simulations have been conducted using computational fluid dynamics (CFD). A CFD simulation was performed by Dong et al. [28], using FLUENT package to study the oscillation of a drop on a substrate subjected to lateral vibration. In this study, however, only the case of immobile contact line was considered. A numerical simulation of static and sliding drop with contact angle hysteresis was performed by Dupont and Legendre [30]. An augmented immersed interface method (IIM) was proposed by Li et al. [31] to simulate liquid drop spreading and recoiling on a solid substrate. The spreading of a droplet in EWOD under DC voltage was simulated by Hong et al. [32], using CFD-ACE$^+$ package in conjunction with a dynamic contact line model. However, drop oscillation under AC voltage was not considered in their study.

As far as we know, there has been no CFD simulation of drop oscillation induced by AC EW. In this paper, we present such a numerical investigation based on an axisymmetric model and the moving mesh interface tracking (MMIT) approach for solving the Navier-Stokes equations. The study focuses on the resonance phenomenon and patterns of oscillation at different forcing frequencies. The MMIT approach is an ideal numerical technique for this study because of its capability in providing a more precise location of the interface.

The rest of this paper is arranged as follows. Sect. 1 presents the mathematical model and numerical method. The validations of the code are given in sect. 2. Sect. 3 describes the results on drop spreading in DC EW and shape oscillation in AC EW. Finally, conclusions are drawn in sect. 4.

1 Mathematical model and numerical method

In this work, we consider the EW-driven spreading and oscillating of a liquid drop in air. Due to the large density ratio of liquid to air in the system, it is justified to use the one-phase free-surface model as a simplified one for the two-phase (liquid-air) problem by neglecting the influence of one phase (air). The droplets are aqueous salt solutions with a radius of the order of 1 mm in most EW experiments. Since the Bond number (which represents the comparison of the strength of gravity and the surface tension) is small, the gravity is also neglected. The movement of the droplet is primarily determined by the surface tension and the electric field applied. From numerical point of view, we need to solve the unsteady Navier-Stokes equations with a moving boundary (free surface). We use a MMIT technique to locate the free surface. Therefore, the computational grids follow the physical interface. Although other methods (level-set method, VOF method, etc.) have proven their high efficiency in simulating fluid flows with moving interfaces, the choice of the moving mesh approach here is motivated by two arguments. First, no topological change is expected to happen in the problem we are dealing with. Second, this technique provides a highly accurate prediction of the free surface. A high precision on the position of the interface is preferable in the moving contact

line simulations.

1.1 Moving-mesh front tracking technique

The MMIT method was proposed by Perot and Nallapati [33] to simulate 2D liquid sloshing and free-surface channel flow. The method uses an exact projection procedure which reduces the number of unknowns as well as satisfying the continuity constraint without solving a pressure Poisson equation. This solution procedure was also analyzed and compared with that in the classic projection methods by Chang et al. [34]. Recently, with a further developed re-meshing capability, this method was used to study more complex problems, such as droplet deformation, collision, jet pinching-off [35–37], etc. A brief introduction to the numerical methodology is given here to make the paper as self-contained as possible. For a more complete description, please refer to the aforementioned papers.

The integral form of the incompressible Navier-Stokes equations in a moving and deforming control volume can be written as:

$$\frac{\mathrm{d}}{\mathrm{d}t}\iiint_{\mathrm{CV}}\mathrm{d}v-\iint_{\mathrm{CS}}\boldsymbol{v}_m\cdot\boldsymbol{n}\mathrm{d}s=0, \tag{1}$$

$$\frac{\mathrm{d}}{\mathrm{d}t}\iiint_{\mathrm{CV}}\rho\mathrm{d}v+\iint_{\mathrm{CS}}\rho(\boldsymbol{u}-\boldsymbol{v}_m)\cdot\boldsymbol{n}\mathrm{d}s=0, \tag{2}$$

$$\frac{\mathrm{d}}{\mathrm{d}t}\iiint_{\mathrm{CV}}\rho\boldsymbol{u}\mathrm{d}v+\iint_{\mathrm{CS}}\rho\boldsymbol{u}(\boldsymbol{u}-\boldsymbol{v}_m)\cdot\boldsymbol{n}\mathrm{d}s=-\iint_{\mathrm{CS}}p\boldsymbol{n}\mathrm{d}s+\iint_{\mathrm{CS}}\mu(\nabla\boldsymbol{u}+\nabla\boldsymbol{u}^{\mathrm{T}})\cdot\boldsymbol{n}\mathrm{d}s. \tag{3}$$

Here $\boldsymbol{u}$ and p are the velocity and pressure; ρ the fluid density; μ the dynamic viscosity; $\boldsymbol{v}_m$ the velocity of the moving mesh. CV and CS are the control volume and control surface respectively. $\boldsymbol{n}$ stands for a normal unit vector which points out of the CS. Eq. (1) is the geometric conservation law (GCL) which simply states that for each control volume, the rate of change of volume must exactly balance the net volume swept due to the motion of its control surfaces. Eqs. (2) and (3) are the continuity and momentum equation, respectively.

The discrete form of the governing equations can be written as:

$$\frac{V_c^{n+1}-V_c^n}{\Delta t}=\sum_f^{\text{cell-faces}}U_f^{\text{mesh}}, \tag{4}$$

$$\sum_f^{\text{cell-faces}}U_f=0, \tag{5}$$

$$\frac{\rho_c^{n+1}\boldsymbol{u}_c^{n+1}V_c^{n+1}-\rho_c^n\boldsymbol{u}_c^nV_c^n}{\Delta t}+\sum_f^{\text{cell-faces}}\rho_f\boldsymbol{u}_f(U_f-U_f^{\text{mesh}})=-V_c^{n+1}(\nabla p)^{n+1}+\sum_f^{\text{cell-faces}}\frac{1}{2}\mu[(\nabla\boldsymbol{u}_f\cdot\boldsymbol{n}A_f)^{n+1}+(\nabla\boldsymbol{u}_f\cdot\boldsymbol{n}A_f)^n] \tag{6}$$

with the definitions of the velocity area integral, mesh velocity area integral and average cell velocity as:

$$U_f=\iint_{\mathrm{CS}}\boldsymbol{u}\cdot\boldsymbol{n}\mathrm{d}s, \tag{7}$$

$$U_f^{\text{mesh}}=\iint_{\mathrm{CS}}\boldsymbol{v}_m\cdot\boldsymbol{n}\mathrm{d}s, \tag{8}$$

$$\boldsymbol{u}_c=\frac{1}{V_c}\iiint_{\mathrm{CV}}\boldsymbol{u}\mathrm{d}v. \tag{9}$$

Here V_c is the volume of a cell and Δt is the time step.

In this numerical scheme, $\boldsymbol{u}_c$ is re-constructed from U_f by

$$\boldsymbol{u}_c=\frac{1}{V_c}\sum_f^{\text{cell-faces}}U_f(\boldsymbol{x}_f-\boldsymbol{x}_c), \tag{10}$$

where $\boldsymbol{x}_f$ and $\boldsymbol{x}_c$ are the position vectors for the centroids of faces and cells, respectively (see Figure 1). Eq. (10) can be written in a matrix notation as $\boldsymbol{u}=V_c^{-1}\boldsymbol{R}U$, where $\boldsymbol{R}$ denotes the 'face-to-cell' operator. Conversely, an integration (or 'cell-to-face') operator can be defined as:

$$W_f=\boldsymbol{w}_{c1}\cdot(\boldsymbol{x}_f-\boldsymbol{x}_{c1})-\boldsymbol{w}_{c2}\cdot(\boldsymbol{x}_f-\boldsymbol{x}_{c2}), \tag{11}$$

where $\boldsymbol{w}_{c1}$ and $\boldsymbol{w}_{c2}$ are two vector quantities defined at centroids of cells and W_f is a scalar quantity defined at centroids of faces. Eq. (11) can also be written in a matrix notation as $W=\boldsymbol{R}^{\mathrm{T}}\boldsymbol{w}$, where $\boldsymbol{R}^{\mathrm{T}}$ is the transpose of $\boldsymbol{R}$.

Eq. (4) is not solved in the computation but acts as a constraint on the mesh velocity $\boldsymbol{v}_m$. In order to be compatible with GCL, the approach suggested by Perot and Nallapati [33] is used to calculate the grid velocity $\boldsymbol{v}_m$. In this approach, the mesh velocity is defined as a constant within the time interval of Δt but varies linearly in space (see Figure 2). The product of the face normal and face area is assumed to vary linearly in time. Thus, each face can be approximated by

$$U_f^{\text{mesh}}\approx\frac{1}{2}(\boldsymbol{v}_{mN_1}+\boldsymbol{v}_{mN_2})\cdot\frac{1}{2}(A_f^{n+1}\boldsymbol{n}_f^{n+1}+A_f^n\boldsymbol{n}_f^n). \tag{12}$$

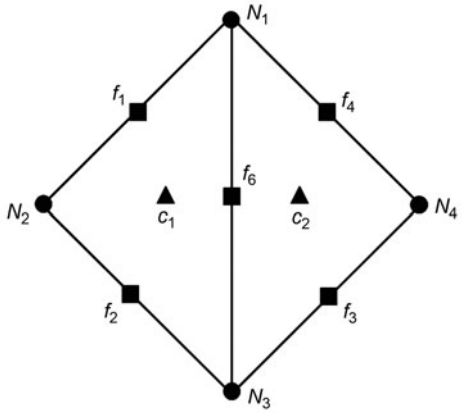

Figure 1 Variable locations on a triangular mesh; $\boldsymbol{u}\rightarrow$ cell (▲); U_f, U_f^{mesh} $\rightarrow$ face (■); $s\rightarrow$ node (●).

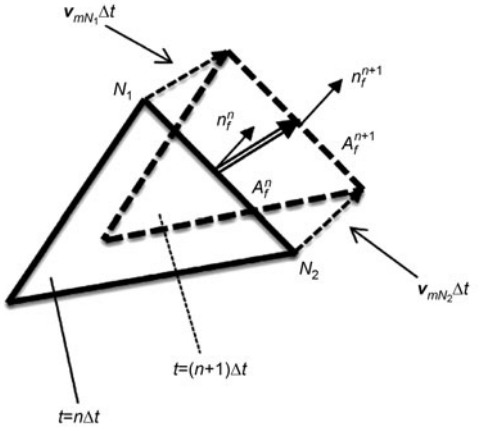

Figure 2 The mesh moving velocity (for each face) which is compatible with GCL.

Here A_f is the face area and $\boldsymbol{n}_f$ is the unit normal vector on the face. $\boldsymbol{v}_{mN_1}$ and $\boldsymbol{v}_{mN_2}$ are the velocities of the two moving nodes associated with the face.

In the MMIT method, the nodes on the free surface move in a Lagrangian fashion and follow the physical motion of the interface. The velocities on these nodes are computed by

$$\frac{\mathrm{d}\boldsymbol{x}_N}{\mathrm{d}t} = \boldsymbol{v}_{m,N} = \frac{1}{N_c}\sum_{c}^{\text{node-cells}} \boldsymbol{u}_c + (\boldsymbol{x}_N - \boldsymbol{x}_c)\cdot\nabla\boldsymbol{u}|_c, \qquad (13)$$

where N_c is the total number of cells associated with one node. To avoid too dense (or sparse) distribution of mesh points on some portions of the free surface, the tangential component (component along the free surface) of the mesh velocity above is modified in some cases, while the vertical motion follows that of the local fluid strictly. The mesh motion in the interior region is chosen somewhat arbitrarily so that the distortion of the computational cells is minimized. For this purpose, the mesh smoothing technique based on the spring analogy [33] has been implemented in this work.

In a matrix form, the discretized eqs. (5) and (6) can be written as:

$$\begin{bmatrix} \left\{\frac{1}{\Delta t}\boldsymbol{M}^{n+1} - \frac{1}{2}(\boldsymbol{R}^{\mathrm{T}})^{n+1}\boldsymbol{L}^{n+1}\right\} & \boldsymbol{G} \\ \boldsymbol{G}^{\mathrm{T}} & 0 \end{bmatrix} \begin{bmatrix} U_f \\ p \end{bmatrix} = \begin{bmatrix} (\boldsymbol{R}^{\mathrm{T}})^{n+1}\dfrac{V^n}{V^{n+1}}\left\{\dfrac{1}{\Delta t}\boldsymbol{u}_c^n - \dfrac{1}{2}\boldsymbol{L}^n + \boldsymbol{N}^{n+1/2}\right\} + f_{\mathrm{surf}} \\ 0 \end{bmatrix}, \qquad (14)$$

where $\boldsymbol{M}^{n+1} = (\boldsymbol{R}^{\mathrm{T}})^{n+1}(\frac{\rho}{V^{n+1}})\boldsymbol{R}^{n+1}$ is the mass matrix; $\boldsymbol{L}$ is the diffusion term and $\boldsymbol{N}$ is the nonlinear convection term. $\boldsymbol{G}$ and $\boldsymbol{G}^{\mathrm{T}}$ are the gradient operator and its transpose respectively. f_{surf} is an additional term on the free surface due to the surface tension force, i.e., $f_{\mathrm{surf}} = \Delta p|_{\text{free-surface}}$. The computation of surface tension will be further discussed in sect. 1.2.

In this method, solving a Poisson equation for the pressure is not required. Instead, the stream-function s is defined at nodes such that $U_f = \boldsymbol{C}s$. Here $\boldsymbol{C}$ is the constructed null space of the gradient operator $\boldsymbol{G}$, such that $\boldsymbol{G}^{\mathrm{T}}\boldsymbol{C} \equiv 0$. By definition, the discrete incompressibility is satisfied to machine precision. By constructing the transpose of $\boldsymbol{C}$ and performing such an operation on the momentum equation, the pressure term can be eliminated and the following equation for s can be obtained,

$$\boldsymbol{C}^{\mathrm{T}}\left\{\frac{1}{\Delta t}\boldsymbol{M}^{n+1} - \frac{1}{2}\boldsymbol{R}^{\mathrm{T}}\boldsymbol{L}^{n+1}\right\}\boldsymbol{C}s^{n+1} = \boldsymbol{C}^{\mathrm{T}}\boldsymbol{R}^{\mathrm{T}}\frac{V^n}{V^{n+1}}\left\{\frac{1}{\Delta t}\boldsymbol{u}_c^n - \frac{1}{2}\boldsymbol{R}^{\mathrm{T}}\boldsymbol{L}^{n+1} + \boldsymbol{N}^{n+1/2}\right\} + \boldsymbol{C}^{\mathrm{T}}f_{\mathrm{surf}}. \qquad (15)$$

This approach also reduces the number of unknowns in the system when the mesh is tetrahedral or triangular, thereby speeding solution times. The system in eq. (15) is symmetric and can be solved using a Jacobi preconditioned conjugate gradient solver.

A three-step second-order, low storage, Runge-Kutta scheme is used for time advancement:

$$\begin{aligned} {\phi_{(1)}}^{n+1} - \phi^n &= \Delta t F(\phi^n), \\ {\phi_{(2)}}^{n+1} - \phi^n &= \Delta t\frac{1}{2}\{F(\phi^n) + F({\phi_{(1)}}^{n+1})\}, \\ \phi^{n+1} - \phi^n &= \Delta t\frac{1}{2}\{F(\phi^n) + F({\phi_{(2)}}^{n+1})\}. \end{aligned} \qquad (16)$$

Due to the explicit treatment of the convective and surface tension term, the time step is limited by the following stability criteria [35]:

$$\Delta t \leqslant \frac{CFL\cdot h}{U}, \qquad (17)$$

$$\Delta t \leqslant C\cdot\sqrt{\frac{\rho h^3}{2\pi\gamma}}, \qquad (18)$$

where γ is the surface tension coefficient between the liquid and the air; h is the grid size; U is the characteristic velocity; CFL and C are two constants of order unity and both are set to 0.5 in this work.

It should be noted that there are some differences in the computational cells (control volumes) for the 2D and the axisymmetric situations (see Figure 3). These differences must be taken into consideration in the discretization procedure, such as the calculation of face areas and cell volumes.

1.2 Boundary conditions and contact line model

There are three types of boundaries in the simulation of axisymmetric droplet spreading: the free surface Γ_1, the fluid-solid interface Γ_2 and the plane of symmetry Γ_3 (see Figure 4). In addition, special treatment is needed to deal with the motion of the contact line (node C) and that of the droplet apex (node S). The boundary conditions are described as follows.

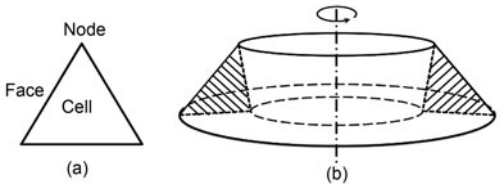

Figure 3 Computational cells used in the finite volume method (FVM) for (a) 2D and (b) axisymmetric situations.

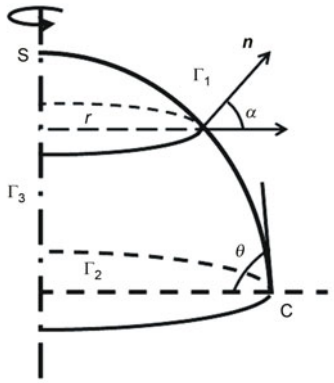

Figure 4 An illustration of an axisymmetric droplet on a solid substrate. Γ_1 represents the free surface; Γ_2 the fluid-solid boundary; Γ_3 the plane of symmetry. The two nodes that need special treatment are the contact line (denoted by C) and the droplet apex (denoted by S).

On the free surface Γ_1, we consider a constant pressure boundary condition outside the free surface. Thus the surface tension is treated as an additional term to the pressure of the boundary (ghost) cell. This additional pressure is computed by

$$\Delta p = \gamma(\kappa_1 + \kappa_2), \tag{19}$$

where κ_1 and κ_2 are the principle curvatures of the liquid-air interface. It is noted that the normal viscous stress term is neglected in the pressure boundary condition (eq. (19)). This is because the capillary number (which represents the relative importance of viscous forces versus surface tension) is much smaller than unity (10^{-4}–10^{-5}) in the present study.

For both two-dimensional and axisymmetric drops, κ_1 is the curvature of a one-dimensional curve. For a two-dimensional drop, κ_2 is zero; while for an axisymmetric drop (see Figure 4), κ_2 is given by

$$\kappa_2 = \frac{\cos\alpha}{r}, \tag{20}$$

where r is the distance to the axis of revolution and α is the angle between the normal vector on the curve and the (positive) horizontal direction.

The curvature κ_1 of the one-dimensional curve is calculated on each segment of the free surface by using a curve-fitting method very similar to that described in the paper by Dai and Schmidt [36]. The only difference is that in the present work, we fit a circle rather than a parabola to a series of points representing the interface.

In the solution procedure, s on the free surface are treated as unknowns and solved (just as the internal nodes) to determine the normal velocity, while for the tangential velocity, the zero-gradient condition is imposed at the "ghost" cells. All the nodes on the free surface (excluding node C and node S) move with the velocity computed by eq. (13) (The tangential component is modified in some cases).

The contact line (node C) is the place where the interfaces of the two fluid phases intersect the solid substrate. In the presence of moving contact lines, the no-slip boundary condition will lead to a non-integrable force singularity. Several different techniques have been proposed to remove this singularity [38–41]. In this paper, the dynamic contact line model developed by Ren et al. [41] is employed. In this model, the mesh velocity of node C is prescribed as a function of the contact angle:

$$u_{\mathrm{cl}} = \frac{\gamma}{\beta_{\mathrm{cl}}}(\cos\theta - \cos\theta_{\mathrm{s}}), \tag{21}$$

where u_{cl} represents the contact line velocity (which is parallel to the solid surface); β_{cl} is the friction coefficient in the contact line region; θ is the dynamic contact angle and θ_{s} the static contact angle.

In this contact line model, the friction coefficient is related to a slip length by

$$\beta_{\mathrm{cl}} = \mu/\ell_{\mathrm{s1}}. \tag{22}$$

The slip length ℓ_{s1} is an important parameter which determines the spreading rate of a drop on a solid substrate. Its effect will be demonstrated by the numerical tests in sect. 2.2.

The change of static contact angle due to the electric field can be predicted by the Lippmann-Young equation

$$\cos\theta_{\mathrm{s}} = \cos\theta_{\mathrm{s0}} + \frac{\varepsilon V(t)^2}{2\gamma d}, \tag{23}$$

where θ_{s0} is Young's angle; ε the permittivity; d the thickness of the insulating layer; V the input electric voltage. Although there is a contact angle saturation at large voltages, the experiment and computation by Oh et al. [10] indicate that no large deviation from the Lippmann-Young equation is found if the voltage is less than 130 V.

On the solid surface Γ_2, s is set to a constant to satisfy the no-penetration condition, while for the tangential component of velocity, the following Navier's slip boundary condition is applied to the ghost cells

$$u = l_{\mathrm{s2}}\frac{\partial u}{\partial y}, \tag{24}$$

where l_{s2} is another slip length for the Γ_2 region.

On the plane of symmetry Γ_3, s is also set to a constant to satisfy the no-penetration condition. This constant should be the same as that on Γ_2 due to the compatibility requirement. In addition, free-slip condition is applied to the tangential component of velocity.

The droplet apex (node S) is the place where the symmetric plane intersects the free surface. For the mesh velocity of node S, the horizontal component should be subtracted from the velocity computed by eq. (13) due to the symmetry condition.

2 Validations

Two validation tests are presented in this section. The first test is the free oscillation of 2D inviscid drop. The numerical results of oscillating frequencies are compared with the theoretical ones. The second test is the axisymmetric spreading of viscous drop on a solid. In this case, in order to match the experimental data, a parameter calibration of the slip length ℓ_{s1} is performed.

2.1 Free oscillation of 2D drop

To validate the solver in handling free surface problem, we simulate the free oscillation of a two-dimensional drop. A 2D inviscid liquid drop is perturbed according to $r = a[1 + \varepsilon\cos(n\theta)]$, where a is the mean radius; ε is a small amplitude of perturbation and n the oscillation mode (see Figure 5). The computational meshes are also shown in this figure. Approximately 2000 elements are used in the simulation. Local mesh refinement is performed near the free surface and coarser meshes are deployed in the interior region.

The theoretical oscillating frequency for mode n is given by

$$\omega = \sqrt{n(n^2-1)\gamma/\rho a^3}. \tag{25}$$

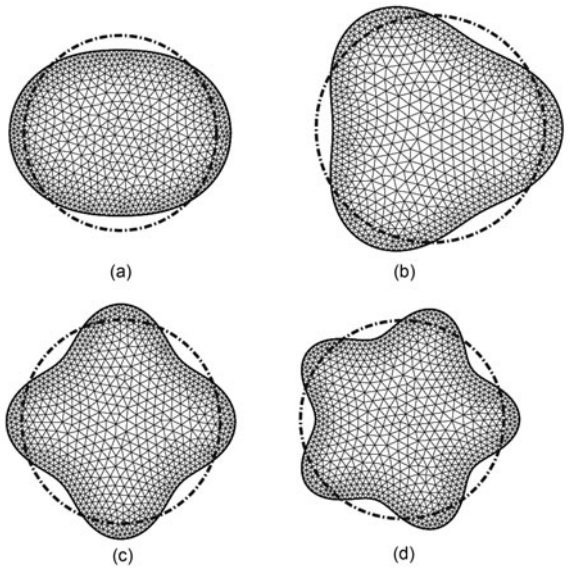

Figure 5 The drop oscillation patterns for four different modes: (a) $n = 2$; (b) $n = 3$; (c) $n = 4$; (d) $n = 5$. The initial shape of the drop is perturbed as $r = a[1 + \varepsilon\cos(n\theta)]$, where ε is set to 0.02 in the simulations and 0.05 for good visualization effect in this figure.

Figure 6 compares the numerical oscillation periods ($T = 2\pi/\omega$) with the theoretical ones, which shows an agreement between them.

2.2 Spreading of axisymmetric drop on solid surface

The objective of this validation is to test the method in handling moving contact lines. For this purpose we consider the partial wetting of an axisymmetric droplet on a solid substrate. The simulations are compared with the experiment conducted by Lavi and Marmur [42] in which they studied a Cyclooctanone drop partially wetting a coated wafer and represented their experimental data by an exponential power law.

In this simulation, the volume of the drop V is 1.75 μL. The initial shape of the drop is a spherical crown with a contact radius of $R_0 = 0.966$ mm. The corresponding initial contact angle is 75°.

The physical properties of the fluid used in the simulation (the same as those in the experiment) are listed in Table 1. As to the slip length ℓ_{s1}, accurate data for realistic substrates/liquids are not easily available. Theoretically speaking, this parameter is introduced in the phenomenological models to remove singularity. Its physical origin is of microscopic nature and its value can possibly be determined by molecular dynamic (MD) simulations [40].

In the numerical simulations, we experimented with different values of ℓ_{s1} and the time histories of wetting area are shown in Figure 7. The contact area is non-dimensionalized using the equilibrium value of the wetting area A_f. $\tau = \frac{\gamma}{\mu V^{1/3}}t$ is the dimensionless time, where V is the volume. From this figure, it is seen that the rate of drop spreading is very sensitive to this parameter. The slip length ℓ_{s1} can thus be tuned to fit the experimental data. Our numerical tests show that the simulation result obtained by setting ℓ_{s1} to be $0.0116R_0$ matches the experimental data reasonably well.

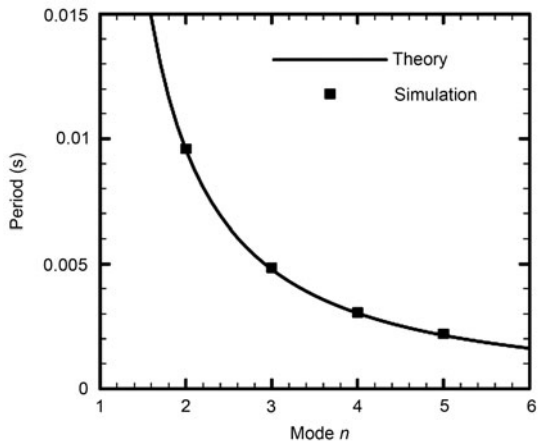

Figure 6 The oscillation periods of an inviscid 2D drop as a function of oscillation mode number. The numerical results are compared with the analytical solutions from eq. (25). In the simulations, the initial shape of the drop is perturbed as $r = a[1 + \varepsilon\cos(n\theta)]$, where ε is set to 0.02.

Table 1 Material properties of the liquid/substrate used in the experiment and simulation of Cyclooctanone drop spreading

Density (kg/m^3)	Viscosity (Pa · s)
974	62.2×10^{-3}
Surface tension (N/m)	Static contact angle (○)
4.1×10^{-2}	54.2

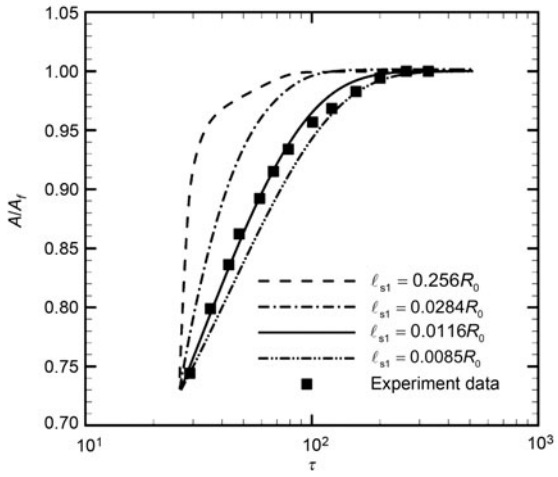

Figure 7 The effect of slip length ℓ_{s1} on the spreading of the drop. The time histories of wetting area obtained by using four different values of ℓ_{s1} ($0.0085R_0, 0.0116R_0, 0.0284R_0$ and $0.256R_0$) are shown in the figure together with the experimental result from Lavi and Marmur [42]. The best fit to the experimental result is obtained by using $\ell_{s1} = 0.0116R_0$.

The effect of the slip length ℓ_{s2} is also tested by varying ℓ_{s2} in the range of $0.0001R_0$–$0.01R_0$ while keeping other parameters unchanged. The results of these simulations are shown in Figure 8. It is seen that the spreading rate is not very sensitive to the selection of ℓ_{s2} in the simulation. The reason for the variation of ℓ_{s2} having little effect on the final results is that the velocity gradient is very small on the substrate (except near the contact line).

Based on the parameter sensitivity tests above, in the study of AC EW that follows, the slip length ℓ_{s1} is first tuned by using the experimental data of DC EW; while ℓ_{s2} is set to $0.001R_0$.

A mesh-independency test has been conducted by performing simulations with four mesh resolutions ($h = 0.09R_0, 0.06R_0, 0.03R_0$, respectively) while keeping other parameters unchange. The result of the test is shown in Figure 9. From this figure, it is seen that there are only minor differences among the solutions. In the subsequent simulations, the mesh size of $h = 0.03R_0$ is used.

3 Results and discussion

In this section, the drop movement induced by EW is studied numerically. We first perform a simulation of drop spreading induced by DC EW. The slip length ℓ_{s1} is calibrated by using the experimental data from Oh et al. [10]. The same slip length is then used in the simulation of AC EW that follows. The mesh resolution used in the simulation is comparable with that described in sect. 2. Careful tests are performed to make sure that the solutions obtained are independent of the mesh size and time step size used. We investigate the response amplitudes of oscillating drop under the input electric frequency ranging from 10 to 230 Hz. The resonance frequencies for different patterns (modes) of oscillation are analyzed and compared with the experimental results from ref. [9].

3.1 Drop spreading driven by DC EW

The experiment data from Oh et al. [10] on drop spreading by DC EW is used to tune the parameter ℓ_{s1}. In their experiment, NaCl solution was used as the conducting liquid and a

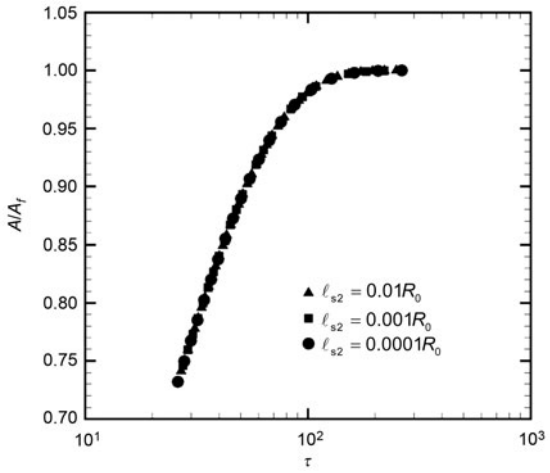

Figure 8 The effect of slip length ℓ_{s2} on the spreading of drop. The time histories of wetting area obtained by using four different values of ℓ_{s2} ($0.0001R_0$, $0.001R_0$, and $0.01R_0$) are shown in the figure. All other parameters are kept the same. The results indicate that the drop spreading rate is not sensitive to this parameter.

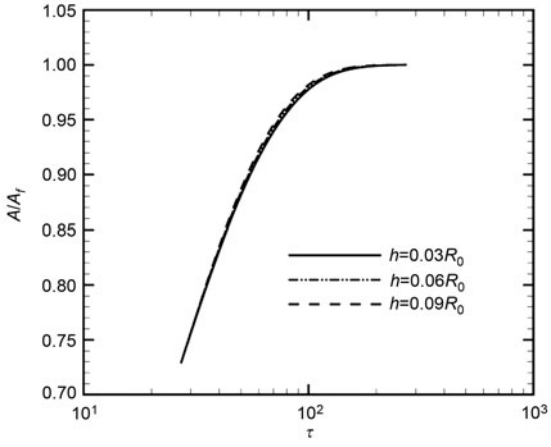

Figure 9 The effect of mesh resolution on the spreading rate of the drop. The time histories of wetting area obtained by using four meshes ($h = 0.09R_0, 0.06R_0, 0.03R_0$, respectively) are shown in this figure. All other parameters are kept the same. It is seen that the mesh-independency is achieved for the mesh resolution in this range.

dielectric layer and a hydrophobic layer were coated on the electrode plate. Some physical properties of the materials used in the experiment (and the simulation) are listed in Table 2. Two different DC voltages, 80 V and 100 V were applied in the experiment.

Figure 10 shows the contact radius as a function of time. It is seen from this figure that a single slip length ($\ell_{s1} = 0.00252R_0$) can be used to reproduce the experimental results for two different electric voltages (80 V and 100 V) with acceptable accuracy. We strongly believe that the slip length ℓ_{s1} is one material property of the substrate/liquid which is not sensitive to the electric voltages applied. Thus in all the simulations of AC EW that follow, the slip length of $0.00252R_0$ is used.

3.2 Drop oscillation driven by AC EW

In this subsection, we study the motion of an aqueous drop in AC EW. The same material properties (those listed in Table 2) are used in the simulation. The input electric voltage is prescribed as:

$$V(t) = \sqrt{2}V_{\rm rms}\sin 2\pi ft, \tag{26}$$

where $V_{\rm rms} = 60$ V and f varies in the range of 10–340 Hz.

3.2.1 Resonance frequencies and patterns of oscillation

The amplitude of drop oscillation, which is defined as the maximum vertical displacement of the drop's apex, is plotted as a function of the input frequency in Figure 11. As shown in this figure, there is an overall trend that the amplitude of oscillation decreases with the increase of input frequency. The local peak amplitudes found in the figure indicate the resonance phenomena at certain frequencies (40, 117, 205 and 300 Hz). The patterns of drop motion at these four frequencies correspond to the oscillation mode of $n = 2, 4, 6, 8$, respectively (see Figure 12). It is interesting to see that the odd modes do not show up in the amplitude-frequency diagram of Figure 11. In the experiment by Oh et al. [9], the odd modes higher than 3 are not observed and the origin of mode 3 is

Table 2 Material properties of the liquid/substrate used in the experiment and simulation of drop spreading and oscillation in DC and AC EW

Density (kg/m^3)	Viscosity (Pa · s)	Surface tension (N/m)
997	0.894×10^{-3}	7.2×10^{-2}
Young's angle (°)	ε_d/d (F/m^2)	Volume (μL)
117	6.62×10^{-6}	5.16

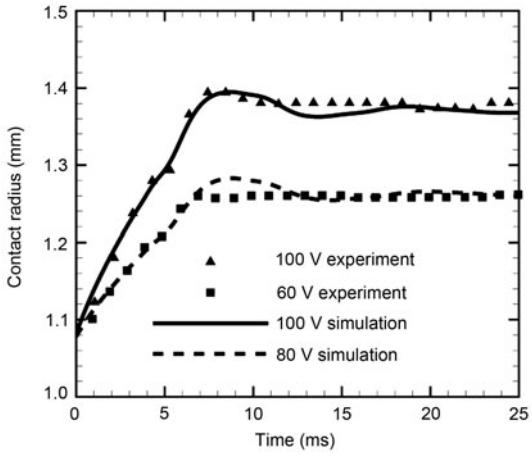

Figure 10 The time variation of contact radius of the drop in the spreading due to 80 V and 100 V DC EW. The numerical results by using a slip length of $\ell_{s1} = 0.00252R_0$ are plotted together with the experimental ones from Oh et al. [10]. It is seen that the numerical simulations can reproduce the experimental results with acceptable accuracy.

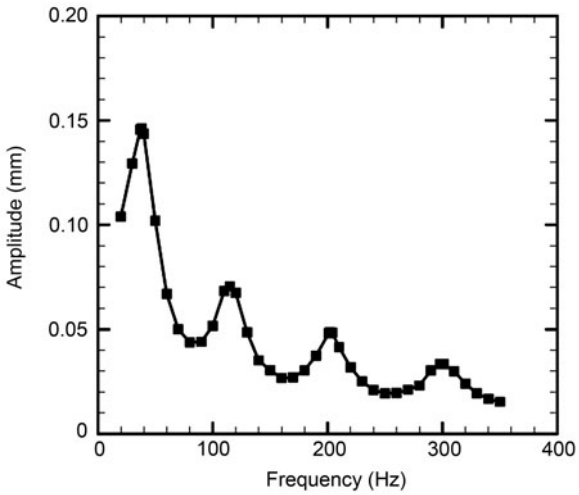

Figure 11 The variation of drop oscillation amplitude with input AC frequency. The rms voltage applied is 60 V. The slip length of $\ell_{s1} = 0.00252R_0$ is used in the simulation. The data obtained in the simulation (those denoted as black squares) are connected by solid lines. Four resonance frequencies (40, 117, 205 and 300 Hz) can be identified from the figure.

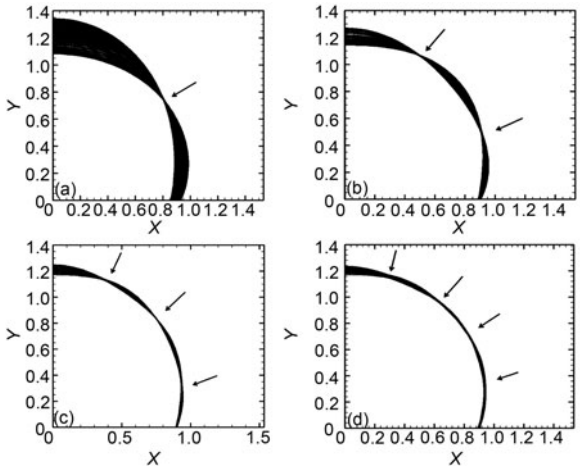

Figure 12 Drop oscillation patterns at the resonance frequencies (a) 40 Hz; (b) 117 Hz; (c) 205 Hz; (d) 300 Hz. Each image is produced by superposing the drop shapes at 25 equally divided time steps in one period. The small arrow plotted in the figure indicates the existence of one node. The oscillation mode can be determined by counting the number of nodes in each image.

conjectured to be the gravitational force acting on the drop. This is consistent with the current numerical result since no gravitational force is included in the simulation.

Table 3 compares the resonance frequencies predicted by the numerical simulation with those by linear analysis and from experiment in Oh et al. [9]. It is seen that for the lower modes (n = 2 and 4), there are relatively larger discrepancies (21% and 17%, respectively) between the numerical results and the experimental ones. The ones predicted by linear analysis is marginally better than the numerical results. For higher modes (n = 6 and 8), however, the numerical simulation gives a better prediction. More specifically, the relative errors in the numerical prediction are 4.6% and 3.8% for mode 6 and mode 8, respectively, while the errors in the prediction by linear analysis are 7.9% and 11.6% for mode 6 and mode 8, respectively. We conjecture that the origin of large discrepancies at lower modes in the present simulation is that the contact line model is inherently flawed. The reason for the reduced discrepancies in higher modes is that the amplitudes of oscillation of the contact line are much smaller. The reason that the numerical simulation gives a better prediction than the linear analysis for high modes is still not clear. One possible reason is the viscous damping effect that is neglected in the linear analysis and this effect becomes larger with the increase of mode number n. However, after further investigation of the formulation for shape mode presented by Oh et al. [9], we find that the modification of the resonance frequency by the damping effect is less than 0.05 Hz for mode 8. We thus believe that the reason for the improved prediction in the present numerical simulation is the inclusion of the nonlinear (convective) term in Navier-Stokes equations, which is neglected in the linear analysis.

The effect of drop volume on the resonance frequency is investigated by studying drops of three different volumes, 4 μL, 8 μL and 12 μL. By applying the AC voltage with $V_{\rm rms}$ = 25 V, the variation of resonance frequency for mode 2 with the increase of drop volume is shown in Figure 13. It is seen that the smaller drop has a higher resonance frequency. The same trend has been observed in the experiments by Sen and Kim [8].

Figure 14 shows the variation of contact radius and contact angle as a function of time at four different input frequencies. From this figure, it is seen that around the resonance frequencies (e.g., 40 and 117 Hz), the contact radius and contact angle are in phase with each other; while away from the resonance frequencies (e.g., 85 and 170 Hz), the contact radius and contact angle are anti-phase. It is interesting to notice that an opposite trend has been found in the experiment by Sen and Kim [8]. The reason for the two conflicting results is still not clear. If we compare the setups of the two experiments by Sen and Kim [8] and by Oh et al. [9], the drop volume, solid substrate and range of electric voltage are all different.

As shown in Figure 14, due to the time-invariant part of the input AC electric field, the static contact angle has been lowered to 105°. With the increase of input frequency, the trend of variation in the oscillation amplitude of contact radius is very similar to that of the drop's apex. A similar trend of variation in the oscillation amplitude for contact angle is also observed in this figure. For example, local peaks of oscillation amplitude for contact angle are reached around the resonance frequencies (12° at 40 and 117 Hz), while nadir values are encountered away from the resonance frequencies (7° at 85 Hz and 4.5° at 170 Hz).

Table 3 Comparisons among the resonance frequencies (Hz) from the present numerical simulation, the linear analysis and the experimental data from Oh et al. [9]

N	Simulation	Linear analysis	Experiment
2	40	38.5	33
4	117	115.6	100
6	205	211.1	196
8	300	322.5	289

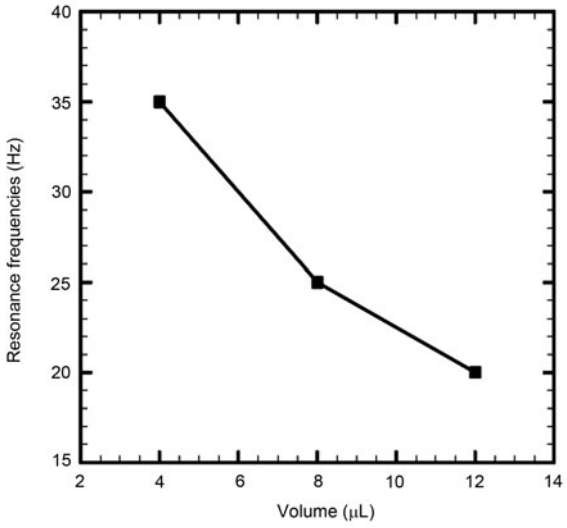

Figure 13 The variation of resonance frequency for mode 2 with drop volume. Drops of three different volumes, 4 μL, 8 μL, 12 μL, under 25 V AC EW are studied. The slip length ℓ_{s1} is set to $0.00252R_0$. The data obtained in the simulation (those denoted as black squares) are connected by solid lines.

3.2.2 *Inclusion of hysteresis into contact line model*

In the previous subsection, the inaccuracy of the contact line model is blamed for the large deviations between the measured and the predicted resonance frequencies for low-mode oscillations. In this subsection, a (supposedly) more accurate contact line model [10,43] which takes into account the contact angle hysteresis is used and the result is compared with that obtained by using the original model.

This more sophisticated model for moving contact line is given by

$$u_{\rm cl} = 0, \text{ if } \theta_{\rm r} < \theta < \theta_{\rm a};$$
$$\gamma(\cos\theta - \cos\theta_s) = \beta_{\rm cl}u_{\rm cl} + \tag{27}$$

$$c_{\text{pin}}\text{sgn}(u_{\text{cl}}) - \frac{c_{\text{pin}}}{\pi/2}\arctan\left(\frac{\beta_{\text{cl}}}{c_{\text{pin}}/(\pi/2)}u_{\text{cl}}\right), \text{otherwise.}$$

The pinning force c_{pin} represents the maximum force that can resist the motion of the drop, whose value is determined from the contact angle hysteresis ($|\cos\theta_s - \cos\theta_{\text{a}}|$ or $|\cos\theta_{\text{r}} - \cos\theta_s|$), where θ_{a} is the advancing angle and θ_{r} is the receding angle. A schematic representation of this model is shown in Figure 15.

A preliminary experiment [10] on DC EW with the electric voltage in the range of 0–140 V showed that the contact angle hysteresis $\theta_{\text{a}} - \theta_{\text{r}}$ varied in between 5° and 20°. In the present study, a 10° contact angle hysteresis is used. In the simulation, in order to properly apply the boundary condition at the moving contact line, the transcendental equation (eq. (27)) is solved at every time step. A bisection method is used to find the root of this equation numerically. The criterion for the iterations to stop is that the error is less than 10^{-8}.

We first perform the simulation of drop spreading driven by DC EW (same as that described in sect. 3.1), but with the contact angle hysteresis. Figure 16 shows the variation of contact radius with time. It is seen from the figure that by including a hysteresis of 10° and using a slip length of $\ell_{\text{s1}} = 0.00361R_0$, there is a perfect match between the numer-

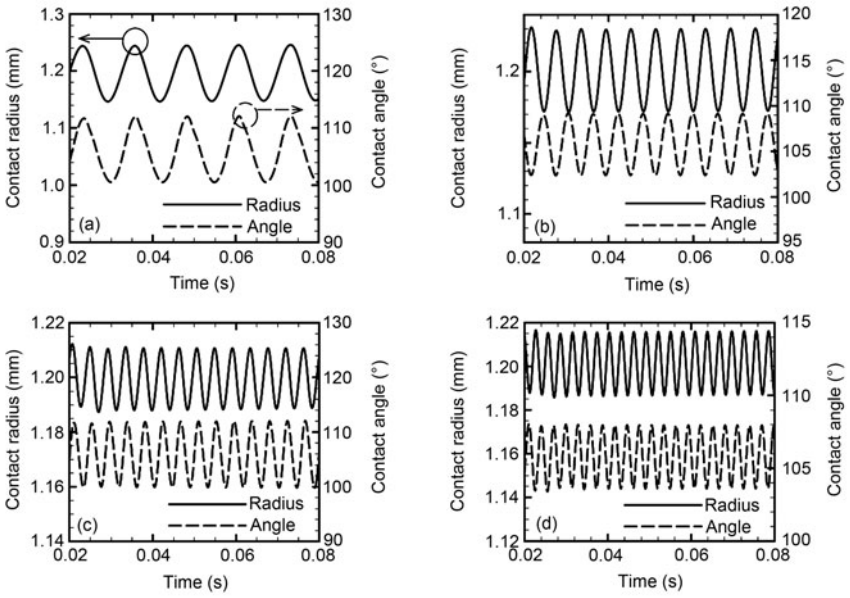

Figure 14 The variation of contact radius and contact angle as a function of time at four different input frequencies: (a) 40 Hz (around the resonance frequency for mode 2); (b) 85 Hz (away from resonance frequencies); (c) 117 Hz (around the resonance frequency for mode 4; (d) 170 Hz (away from resonance frequencies).

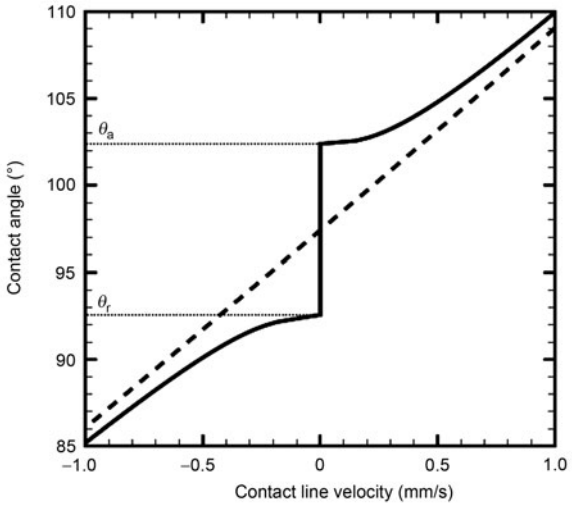

Figure 15 A schematic representation of the contact line model in which the contact angle hysteresis is included. The solid line denotes the more sophisticated model and the dashed line denotes the original model without hysteresis. Please note that the solid line asymptotes towards the dashed line.

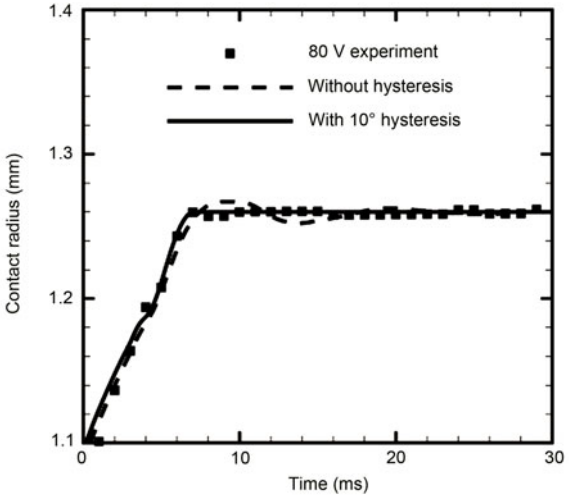

Figure 16 The variation of contact radius as a function of time for a 5 μL drop in the spreading due to 80 V AC EW and the comparison of results with and without contact angle hysteresis. The numerical result by including a 10° contact angle hysteresis and using a slip length of $\ell_{\text{s1}} = 0.00361R_0$ perfectly matches the experimental one.

ical and the experimental results. Compared with that obtained without including the hysteresis (the one obtained in sect. 3.1), the discrepancy between the numerical and the experimental results is further reduced by using the new model. Thus, in the simulation of AC EW that follows, the slip length of $0.00361R_0$ is used in conjunction with the contact angle hysteresis of 10°.

Figure 17 shows the time history of contact radius and contact angle for the input frequency of 37 Hz, with the inclusion of hysteresis. Compared with Figure 14, the effect of hysteresis is clearly seen in the form of stops (sticks) in the time history of contact radius and the multiperiodic nature of the time history of contact angle. Similar features have also been observed in the experiment by Sen and Kim [8].

The amplitude-frequency diagram with the inclusion of contact angle hysteresis is shown in Figure 18. It is seen that all resonance frequencies are shifted towards the lower side when the contact angle hysteresis is included into the model. However, the trend of variation of the oscillation amplitude (at the resonance frequencies) with the inclusion of hysteresis is quite complicated. For modes 2, 4 and 6, the oscillation amplitude is reduced, while for mode 8, the amplitude is enhanced if compared with the one without hysteresis. The increase of oscillation amplitudes due to contact angle hysteresis is against our intuition since the hysteresis is normally considered as an extra friction on the contact line.

The predicted resonance frequencies using the sophisticated model are summarized in Table 4, where the comparisons with the results from the original model and from the experiment are made. It is seen that the inclusion of hysteresis significantly improves the prediction. The relative error in the predicted resonance frequency has been reduced from 21% to 12% for mode 2; from 17% to 11% for mode 4. For the higher modes (6 and 8), there is a perfect match between the predicted values and the ones measured in the experiment.

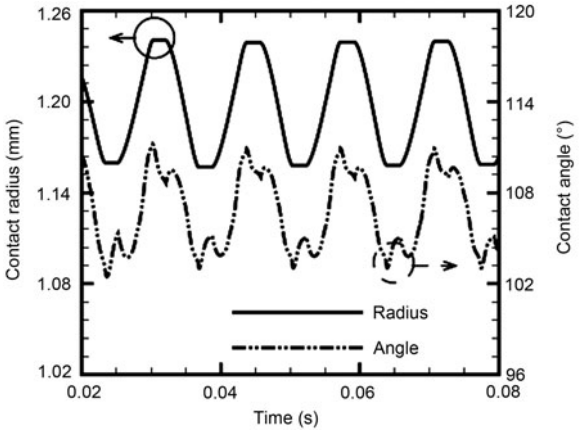

Figure 17 The variations of contact radius and contact angle as a function of time at the input frequency of 37 Hz. The simulation is performed by using the contact line model which includes the contact angle hysteresis of 10°. Effect of the contact angle hysteresis can be clearly seen in the figure in the form of stops (sticks) in the time history of contact radius and multiperiodic feature in the time variation of contact angle.

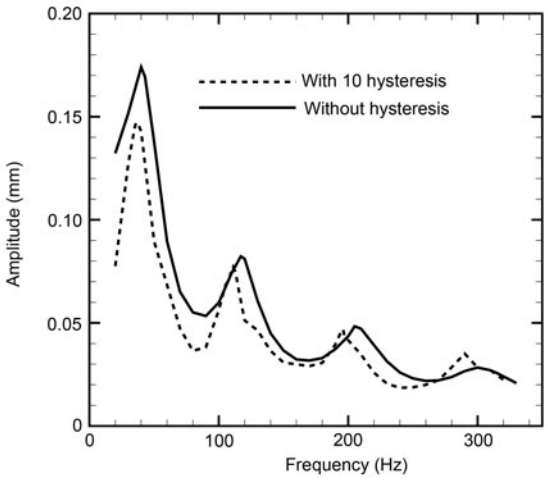

Figure 18 The amplitude-frequency diagram with and without the inclusion of contact angle hysteresis. By including the contact angle hysteresis, the resonance frequencies for all modes are shifted to the lower side. The oscillation amplitude is reduced for modes 2, 4, 6; but enhanced for mode 8.

Table 4 Comparisons among the resonance frequencies (Hz) predicted by using the more sophisticated model and the original model and the ones from the experiment by Oh et al. [9]

N	No hysteresis	With 10° hysteresis	Experiment
2	40	37	33
4	117	111	100
6	205	196	196
8	300	289	289

4 Conclusions

The drop oscillation driven by AC EW is investigated numerically by using an axisymmetric model in conjunction with the MMIT method and the contact line model proposed by Ren et al. [41]. We studied the patterns of drop oscillation at the AC electric voltage of $V_{\rm rms} = 60$ V with the input frequency ranging from 10 to 330 Hz. When we compare the experimental results, a reasonably good prediction of resonance frequencies for different modes has been achieved. The discrepancy between the experimental result and the present simulation can be further reduced by using a more sophisticated contact line model which includes the contact angle hysteresis.

There are two important dimensionless parameters which characterize the relative importance of inertial, viscous and surface tension forces in this problem: the Reynolds number ($Re = (\rho u_{\rm cl} R_0)/\mu$) and the Weber number ($We = (\rho u_{\rm cl}^2 R_0)/\gamma$). In the present study, the Re number is in the range of 10–100 and the We number is of the order of 10^{-2}. The implications of this parameter range are as follows. First, in this range of Re number, the validity of linearized models is dubious. Second, this type of flow is clearly dominated by surface tension.

To achieve a prediction which can be used to aid the design of EW-based devices, an accurate value of the slip length in the contact line model is the key to success. For realistic liquid/substrate, this parameter is not easily available and it

can only be determined through a calibration process using some experimental data. In the present work, this parameter is tuned using the data from the experiment of drop spreading driven by DC EW. A noticeable improvement has been made in the prediction of resonance frequencies by including the contact angle hysteresis into the model. Note that the prediction error can be further reduced by using a more accurate value of contact angle hysteresis and more carefully designed calibration process (such as some optimization algorithms) other than the crude trial and error method used here. Also, it should be noted that other dynamic models for moving contact line [39,44–47] can be readily incorporated into our numerical method.

This work was supported by the Chinese Academy of Sciences (Grant Nos. KJCX-SW-L08, KJCX2-YW-H18 and KJCX3-SYW-S01), the National Basic Research Program of China (Grant No. 2007CB814803) and the National Natural Science Foundation of China (Grant Nos. 10732090, 10872201 and 11023001).

1 Kang K H. How electrostatic fields change contact angle in electrowetting. Langmuir, 2002, 18: 10318–10322
2 Mugele F, Baret J C. Electrowetting: From basics to applications. J Phys-Condens Matter, 2005, 17: 705–774
3 Pollack M G, Fair R B, Shenderov A D. Electrowetting-based actuation of liquid droplets for microfluidic applications. Appl Phys Lett, 2000, 77: 1725–1726
4 Pollack M G, Shenderov A D, Fair R B. Electrowetting-based actuation of droplets for integrated microfluidics. Lab Chip, 2002, 2: 96–101
5 Hayes R A, Feenstra B J. Video-speed electronic paper based on electrowetting. Nature, 2003, 425: 383–385
6 Krupenkin T, Yang S, Mach P. Tunable liquid microlens. Appl Phys Lett, 2003, 82: 316–318
7 Huh D, Tkaczyk A H, Bahng J H. Reversible switching of high-speed air-liquid two-phase flows using electrowetting-assisted flow pattern change. J Am Chem Soc, 2003, 125: 14678–14679
8 Sen P, Kim C J. A fast liquid-metal droplet microswitch using EWOD-driven contact-line sliding. J Microelectromech S, 2009, 18: 174–185
9 Oh J M, Ko S H, Kang K H. Shape oscillation of a drop in ac electrowetting. Langmuir, 2008, 24: 8379–8386
10 Oh J M, Ko S H, Kang K H. Analysis of electrowetting-driven spreading of a drop in air. Phys Fluids, 2010, 22: 032002
11 Sen P, Kim C J. Capillary spreading dynamics of electrowetted sessile droplets in air. Langmuir, 2009, 25: 4302–4305
12 Decamps C, Coninck J D. Dynamcis of spontaneous spreading under electrowetting conditions. Langmuir, 2000, 16: 10150–10153
13 Ko S H, Lee H, Kang K H. Hydrodynamic flows in electrowetting. Langmuir, 2008, 24: 1094–1101
14 Garcia-Sanchez P, Ramos A, Mugele F. Electrothermally driven flows in ac electrowetting. Phys Rev E, 2010, 81: 0153039(R)
15 Lee H, Yun S, Ko S H. An electrohydrodynamic flow in ac electrowetting. Biomicrofluidics, 2009, 3: 044113
16 Baret J C, Decre M M J, Mugele F. Transport dynamics in open microfluidic grooves. Langmuir, 2007, 23: 5200–5204
17 Cooney C G, Chen C Y, Emerling M R, et al. Electrowetting droplet microfluidics on a single planar surface. Microfluid Nanofluid, 2006, 2: 435–446
18 Chung S K, Zhao Y, Yi U C, Separation and collection of microparticles using oscillating bubbles. In: the 20th International Conference on Micro Electro Mechanical Systems. Hyogo: IEEE, 2007. 21–25
19 Gunji M, Washizu M J. Self-propulsion of a water droplet in an electric field. J Phys D-Appl Phys, 2005, 38: 2417–2423
20 Mugele F, Baret J C, Steinhauser D. Microfluidic mixing through electrowetting-induced droplet oscillations. Appl Phys Lett, 2006, 88: 204106
21 Blake T D, Clarke A, Stattersfield E H. An investigation of electrostatic assist in dynamic wetting. Langmuir, 2000, 16: 2928–2935
22 Gabay C, Berge B, Dovillaire G, et al. Dynamic study of a varioptic variable focal lens. Proc SPIE, 2002, 4767: 159–165
23 Rayleigh L. On the capillary phenomena of jets. Proc R Soc London, 1879, 29: 71–79
24 Lamb H. Hydrodynamics. 6th ed. Cambridge: Cambridge University Press, 1932
25 Strani M, Sabetta F. Free vibrations of a drop in partial contact with a solid support. J Fluid Mech, 1984, 141: 233–247
26 Noblin X, Buguin A, Brochard-Wyart F. Self-propulsion of a water droplet in an electric field. Eur Phys J E, 2004, 14: 395–404
27 Noblin X, Buguin A, Brochard-Wyart F. Triplon modes of puddles. Phys Rev Lett, 2005, 94: 166102
28 Dong L, Chaudhury A, Chaudhury M K. Lateral vibration of a water drop and its motion on a vibrating surface. Eur Phys J E, 2006, 21: 231–242
29 Fayzrakhmanova I S, Straube A V. Stick-slip dynamics of an oscillated sessile drop. Phys Fluids, 2009, 21: 072104
30 Dupont J B, Legendre D. Numerical simulation of static and sliding drop with contact angle hysteresis. J Comput Phys, 2010, 229: 2453–2478
31 Li Z L, Lai M C, He G W, et al. An augmented method for free boundary problems with moving contact lines. Comput Fluids, 2010, 39: 1033–1040
32 Hong F J, Cheng P, Sun Z, et al. Simulation of spreading dynamics of a EWOD droplet with dynamic contact angle and contact angle hysteresis. In: Proceedings of the ASME 2009 Second International Conference on Micro/Nanoscale Heat and Mass Transfer, 2009. MNHMT2009-18558: 635–641
33 Perot B, Nallapati R. A moving unstructured staggered mesh method for the simulation of incompressible free-surface flows. J Comput Phys, 2003, 184: 192–214
34 Chang W, Giraldo F, Perot B. Analysis of an exact fractional step method. J Comput Phys, 2002, 180: 183–199
35 Dai M Z, Wang H, Perot B, et al. Direct interface tracking of droplet deformation. Atomiz Spr, 2002, 12: 721–736
36 Dai M Z, Schmidt D P. Adaptive tetrahedral meshing in free-surface flow. J Comput Phys, 2005, 208: 228–252
37 Quan S P, Schmidt D P. A moving mesh interface tracking method for 3D incompressible two-phase flows. J Comput Phys, 2007, 221: 761–780
38 Anderson D M, McFadden G B, Wheeler A A. Diffusive-interface method in fluid mechanics. Annu Rev Fluid Mech, 1998, 30: 139–165
39 Dussan E B. On the shredding of liquids on solid surfaces: Static and dynamic contact lines. Annu Rev Fluid Mech, 1979, 11: 371–400
40 Ren W, E W. Boundary conditions for the moving contact line problem. Phys Fluids, 2007, 19: 022101
41 Ren W, Hu D, E W. Continuum models for the contact line problem. Phys Fluids, 2010, 22: 102103
42 Lavi B, Marmur A. The exponential power law: Partial wetting kinetics and dynamic contact angles. Colloid Surf A, 2004, 250: 409–414
43 Walker S W, Shapiro B, Nochetto R H. Electrowetting with contact line pinning: Computational modeling and comparisons with experiments. Phys Fluids, 2009, 21: 102103
44 Tanner L H. The spreading of silicone oil drops on horizontal surfaces. J Phys D-Appl Phys, 1979, 12: 1473–1484
45 De Gennes P G, Hua X, Levinson P. Dynamics of wetting: Local contact angles. J Fluid Mech, 1990, 212: 55–63
46 Cox R G. Inertial and viscous effects on dynamic contact angles. J Fluid Mech, 1998, 357: 249–278
47 Eggers J. Toward a description of contact line motion at higher capillary numbers. Phys Fluids, 2004, 16: 3491–3494